Materials Horizons

ROYAL SOCIETY OF CHEMISTRY

COMMUNICATION

View Article Online
View Journal | View Issue

Check for updates

Cite this: *Mater. Horiz.*, 2021, 8, 1264

Received 1st December 2020,
Accepted 22nd January 2021

DOI: 10.1039/d0mh01921f

rsc.li/materials-horizons

Published on 23 1 2021. Downloaded on 2024-08-16 4:52:42.

A multifunctional Fenton nanoagent for microenvironment-selective anti-biofilm and anti-inflammatory therapy†

Yuqing Li,[a] Weijun Xiu,[a] Kaili Yang,[a] Qirui Wen,[a] Lihui Yuwen,*[a] Zichao Luo,[b] Xiaogang Liu,[b] Dongliang Yang,[c] Xiaoji Xie[d] and Lianhui Wang*[a]

Bacterial biofilm infections are intractable to traditional antibiotic treatment and usually cause persistent inflammation. Chemodynamic therapy (CDT) based on the Fenton reaction has recently emerged as a promising anti-biofilm strategy. However, the therapeutic efficacy of current Fenton agents often suffers from inefficient Fenton activity and lacks anti-inflammatory capability. Herein, $FePS_3$ nanosheets (NSs) are explored for the first time as novel microenvironment-selective therapeutic nanoagents for bacterial biofilm infections with both self-enhanced Fenton activity for an anti-biofilm effect and reactive oxygen species (ROS) scavenging properties for an anti-inflammatory effect. In biofilms with acidic microenvironments, $FePS_3$ NSs release Fe^{2+} to generate toxic ROS by Fenton reaction and reductive $[P_2S_6]^{4-}$ to enhance the Fenton activity by reducing Fe^{3+} to Fe^{2+}. In the surrounding normal tissues with neutral pH, $FePS_3$ NSs scavenge ROS by reductive $[P_2S_6]^{4-}$ with an anti-inflammatory effect. This work demonstrates multifunctional Fenton nanoagents with microenvironment-selective ROS generation and elimination properties for effective treatment of bacterial biofilm infections with both anti-biofilm and anti-inflammatory effects.

New concepts

Fenton agents catalytically convert hydrogen peroxide (H_2O_2) to highly oxidative hydroxyl radicals (•OH) for effective bacteria-killing without common drug-resistance issues. However, their therapeutic efficacy for bacterial biofilm infections is usually confronted with two challenges: (i) the low iron redox cycling efficiency from Fe^{3+} to Fe^{2+} limits the Fenton reaction activity and •OH formation, resulting in inefficient biofilm eradication. (ii) Current Fenton agents lack microenvironment-selective reactive oxygen species (ROS) regulation capability, which restrains their use only for ROS generation to kill bacteria in biofilms rather than ROS elimination to mitigate inflammation in normal tissues. Herein, a novel multifunctional Fenton nanoagent ($FePS_3$ nanosheets, $FePS_3$ NSs) is firstly demonstrated to possess both self-enhanced Fenton activity in biofilm infected tissues with acidic pH and ROS scavenging properties in normal tissues with neutral pH. The microenvironment-selective ROS regulation properties of $FePS_3$ NSs originates from the integration of Fenton-active Fe cations and reductive $[P_2S_6]^{4-}$ anions. Overall, this work not only offers an effective therapeutic method for the treatment of bacterial biofilm infections with both anti-biofilm and anti-inflammatory effects, but also inspires the rational design of multifunctional Fenton nanoagents by integrating Fenton-active cations and reductive anions.

Bacterial infections have emerged as ever-growing threats to human health, and many recalcitrant bacterial infections have been proven to correlate with the formation of biofilms, such as lung infections in cystic fibrosis, implant-related infections, chronic wounds, dental caries, and so on.[1–3] A bacterial biofilm is an aggregate of bacterial populations encapsulated in the extracellular polymeric substance (EPS) matrix, which can protect bacteria from the attack of host immune defenses and cause high resistance to antibiotics.[4–6] Furthermore, persistent inflammation is often caused by bacterial biofilm infection, which can damage the surrounding normal tissues and hamper the recovery of infected tissues.[7–9] To date, the effective treatment of bacterial biofilm infections is still highly desired, especially a method with both anti-biofilm and anti-inflammatory effects.

CDT based on Fenton/Fenton-like reactions has recently been considered a promising therapeutic strategy for the treatment of cancer and bacterial infections.[10–14] Fenton agents catalytically convert hydrogen peroxide (H_2O_2) to highly oxidative hydroxyl radicals (•OH), which irreversibly damage various

[a] *Key Laboratory for Organic Electronics and Information Displays & Jiangsu Key Laboratory for Biosensors, Institute of Advanced Materials (IAM) & Jiangsu National Synergetic Innovation Centre for Advanced Materials (SICAM), Nanjing University of Posts and Telecommunications, Nanjing 210023, China. E-mail: iamlhyuwen@njupt.edu.cn, iamlhwang@njupt.edu.cn*

[b] *Department of Chemistry, National University of Singapore, Singapore 117543, Singapore*

[c] *Institute of Advanced Materials (IAM), School of Physical and Mathematical Sciences, Nanjing Tech University, Nanjing 211800, China*

[d] *Institute of Advanced Materials (IAM), Jiangsu National Synergetic Innovation Centre for Advanced Materials (SICAM), Nanjing Tech University, Nanjing 211800, China*

† Electronic supplementary information (ESI) available. See DOI: 10.1039/d0mh01921f

This journal is © The Royal Society of Chemistry 2021

Published on 23 1 2021. Downloaded on 2024-08-16 4:52:42.

biomolecules (proteins, lipids, DNA, *etc.*) and effectively kill drug-resistant cancer cells or bacteria.[10,15–20] Various Fenton agents have been used to kill bacteria both in planktonic form and in biofilms.[21–24] However, the anti-biofilm effect of Fenton agents is limited by the inefficient iron redox cycling and •OH production, because the reduction of the as-formed Fe^{3+} to Fe^{2+} by H_2O_2 is much slower than the oxidation of Fe^{2+}.[25–27] Although chelating agents or reductive agents can improve the iron redox cycling during Fenton reaction, they are complicated and unstable for biological use.[28–30] On the other hand, common Fenton agents lack the anti-inflammatory capability to scavenge excessive ROS accumulated in the normal tissues around biofilms.[31,32] Hence, Fenton agents with enhanced iron redox cycling and ROS scavenging activity are highly desired to treat bacterial biofilm infections.

In bacterial biofilm infected tissues, interactions between the bacteria and the host result in unique biofilm microenvironments.[9,33,34] The respiratory burst of abundant phagocytes around bacterial biofilms results in high levels of ROS (*e.g.*, H_2O_2) in biofilm infected tissues.[35,36] Besides, bacteria in oxygen-limited regions of the biofilm conduct anaerobic fermentation along with the accumulation of organic acids, which causes a more acidic microenvironment in biofilm infected tissues compared with neutral normal tissues.[37,38] By utilizing the biofilm microenvironment as a stimulus, responsive nanoagents have shown selective anti-biofilm outcomes with diminished side effects to normal tissues.[39–46] Inspired by these reports, we expect that $FePS_3$ NSs have potential as microenvironment-selective therapeutic agents for biofilm infections based on the existence of both Fenton-active Fe cations (Fe^{2+}/Fe^{3+}) for bacterial killing and reductive anions ($[P_2S_6]^{4-}$) for ROS scavenging.

$FePS_3$ NSs were prepared from bulk $FePS_3$ by ball-milling and subsequent ultrasonic exfoliation (Scheme 1). $FePS_3$ NSs exhibit acid-responsive dissociation with the release of Fe^{2+} and $[P_2S_6]^{4-}$ while being relatively stable under neutral conditions. In bacterial biofilm infected tissues with acidic pH, the released Fe^{2+} further converts H_2O_2 to •OH through Fenton reaction, and the $[P_2S_6]^{4-}$ can reduce the as-formed Fe^{3+} to Fe^{2+} with accelerated iron redox cycling and enhance the Fenton activity. In contrast, in normal tissues with neutral pH, $FePS_3$ NSs show antioxidative activity and can effectively scavenge H_2O_2 or •OH by the reductive $[P_2S_6]^{4-}$ through redox reaction. Experimental results show that the microenvironment-selective ROS regulation properties of $FePS_3$ NSs enable simultaneous anti-biofilm and anti-inflammatory therapy for bacterial biofilm infections.

Bulk $FePS_3$ was synthesized by high temperature solid state reaction using Fe, P, and S powders.[47] The scanning electron microscopy (SEM) image (Fig. S1a, ESI†) shows clear layered morphology of bulk $FePS_3$. The X-ray diffraction (XRD) pattern (Fig. S1b, ESI†) further confirms the successful synthesis of bulk $FePS_3$. $FePS_3$ NSs were obtained by ball-milling and subsequent liquid ultrasonication of the bulk $FePS_3$ with the assistance of poly(vinyl pyrrolidone) (PVP). The transmission electron microscopy (TEM) image (Fig. 1a) and the statistical analysis (Fig. S2a, ESI†) illustrate that $FePS_3$ NSs have uniform morphology with an average size of ~15 nm. Dynamic light scattering (DLS) analysis shows that the hydrodynamic diameter of $FePS_3$ NSs is around 24 nm (Fig. S2b, ESI†). As the high-resolution TEM (HRTEM) image shows in Fig. 1b, the crystal lattice space of 1.86 Å can be ascribed to the (310) plane of $FePS_3$. High-angle annular dark field scanning TEM (HAADF-STEM) image and energy dispersive spectroscopy (EDS) elemental mapping images (Fig. 1c) show the homogeneous element distribution of Fe, P, and S in $FePS_3$ NSs. Atomic force microscopy (AFM) measurement (Fig. 1d and Fig. S2c, ESI†) indicates the average thickness of $FePS_3$ NSs to be ~2.1 nm, suggesting that $FePS_3$ NSs have 2–3 single layers.[48] Besides, $FePS_3$ NSs have negative charges on the surface with a zeta potential of about −10 mV (Fig. S2d, ESI†).

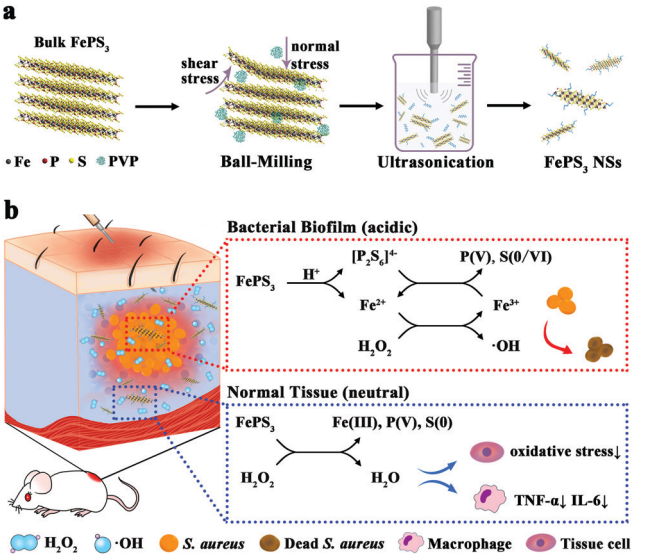

Scheme 1 (a) Preparation of $FePS_3$ NSs by ball-milling and ultrasonication method. (b) $FePS_3$ NSs exhibit both self-enhanced Fenton activity in biofilm infected tissues with acidic pH for the eradication of biofilms and ROS scavenging properties in normal tissues with neutral pH for the remission of inflammation.

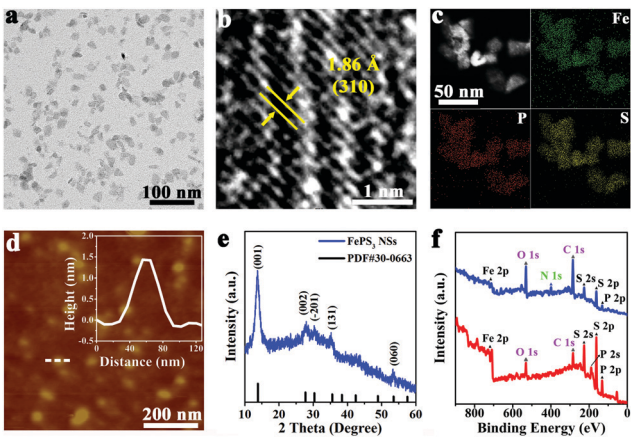

Fig. 1 (a) TEM image, (b) HRTEM image, (c) HAADF-STEM image and the corresponding EDS elemental mapping images, (d) AFM image with height profile, and (e) XRD pattern of $FePS_3$ NSs. (f) XPS survey spectra of $FePS_3$ NSs (blue) and bulk $FePS_3$ (red).

Published on 23 1 2021. Downloaded on 2024-08-16 4:52:42.

As the XRD pattern shows in Fig. 1e, the diffraction peaks of $FePS_3$ NSs located at 13.8° and 27.8° can be ascribed to (001) and (002) planes of $FePS_3$, respectively. Fig. S3a (ESI†) shows that $FePS_3$ layers are formed by $[P_2S_6]^{4-}$ units and Fe ions, and then weakly bond with each other through van der Waals forces.[49] The Raman spectrum of $FePS_3$ NSs (Fig. S3b, ESI†) exhibits a peak at 385 cm^{-1} ($A_{1g}^{(2)}$), which represents P–P bond stretching and the symmetric stretching vibration of the P–S bond in the $[P_2S_6]^{4-}$ unit. Raman peaks at 215 cm^{-1} ($E_g^{(1)}$), 275 cm^{-1} ($E_g^{(2)}$), and 588 cm^{-1} ($E_g^{(3)}$) originate from the tangential vibration of the P–P bond, which suggests the inplane vibrations of the $[P_2S_6]^{4-}$ unit.[48] Fourier transform infrared (FT-IR) spectra in Fig. S3c (ESI†) show the asymmetric stretching vibration of the P–S bond (572 cm^{-1}) and the P–P vibration (442 cm^{-1}) of $FePS_3$.[50,51] IR bands at 1642 cm^{-1} and 1428 cm^{-1} belong to the stretching vibration of amide C=O and the C–H bending vibration, respectively, suggesting the presence of PVP on $FePS_3$ NSs.

$FePS_3$ NSs were further characterized by using X-ray photoelectron spectroscopy (XPS). XPS survey spectra show that $FePS_3$ NSs and bulk $FePS_3$ have similar binding energy peaks of the main elements, while the N 1s peak for $FePS_3$ NSs can be ascribed to the surface adsorbed PVP (Fig. 1f). As the high-resolution XPS spectra of Fe 2p show in Fig. S4a (ESI†), the binding energies of $2p_{3/2}$ and $2p_{1/2}$ orbitals of Fe(II) are 709.3 eV and 722.9 eV, respectively.[52] And the peaks near 712.0 eV and 725.6 eV belong to the $2p_{3/2}$ and $2p_{1/2}$ orbitals of Fe(III), indicating the coexistence of Fe(II) and Fe(III) on the surface of bulk $FePS_3$ and $FePS_3$ NSs, similar to the reported results.[47] Also, the main P 2p peaks located at 131.1 eV ($2p_{3/2}$) and 132.0 eV ($2p_{1/2}$) represent the intrinsic valence state of +4 for P in $FePS_3$. Additional peaks at 132.8 eV and 133.7 eV for P 2p suggest partial oxidation of P, which may originate from the preparation process (Fig. S4b, ESI†).[53] Besides, no obvious difference of S 2p binding energy peaks can be observed between $FePS_3$ NSs and bulk $FePS_3$ (Fig. S4c, ESI†). Moreover, the peaks at 188.7 eV and 225.6 eV represent the P 2s and S 2s orbitals of $FePS_3$, respectively; whereas the C 1s peak (284.6 eV) and O 1s peak (531.6 eV) may originate from the test environment (Fig. 1f).

The existence of Fe(II) in $FePS_3$ NSs indicates their potential Fenton activity, whereas the $[P_2S_6]^{4-}$ may possess reducibility due to the low valence states of P and S (+4 and −2, respectively). First of all, 3,3′,5,5′-tetramethylbenzidine (TMB) was used as the substrate to carry on the colorimetric assay of Fenton activity.[54] As shown in Fig. 2a, the characteristic absorbance at 652 nm increases significantly with the decrease of pH, while no obvious change is observed at pH 7.4, indicating that $FePS_3$ NSs exhibit Fenton activity only under acidic conditions. Moreover, the generation of $^{\bullet}OH$ in these reactions was further detected by electron paramagnetic resonance (EPR) by using 5,5-dimethyl-1-pyridine *N*-oxide (DMPO) as the spin trap.[55] Fig. 2b shows obvious DMPO/$^{\bullet}OH$ signals for $FePS_3$ NSs + H_2O_2 mixture at pH 5.0, while no characteristic signal appears at pH 7.4, which further verifies the acid-responsive Fenton activity of $FePS_3$ NSs.

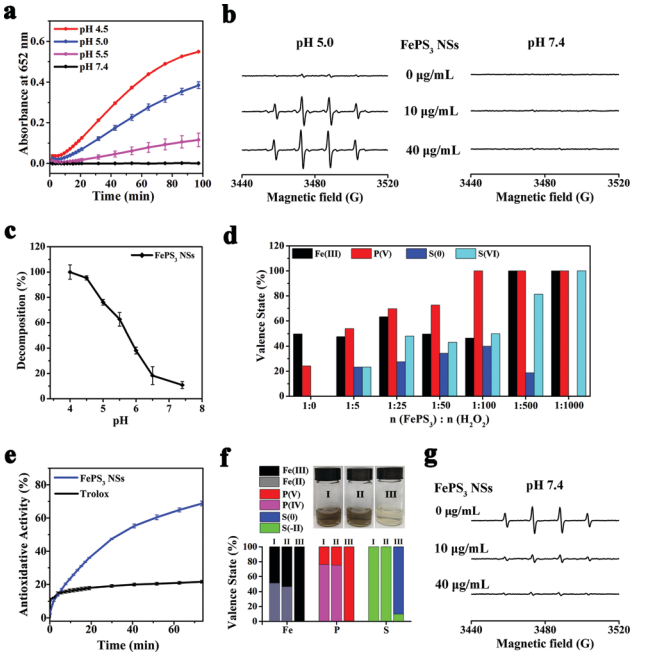

Fig. 2 (a) Fenton activity of $FePS_3$ NSs characterized using TMB assay (TMB + H_2O_2 + $FePS_3$ NSs) under different pH conditions. (b) EPR spectra of the DMPO + H_2O_2 mixtures with $FePS_3$ NSs at different concentrations and different pH conditions. (c) Dissolution of $FePS_3$ NSs in phosphate buffer solutions (PBS) under different pH conditions after incubation for 6 h. (d) Percentage of Fe, P, and S at various valence states in $FePS_3$ NSs after being incubated with different amounts of H_2O_2 at pH 5.0. (e) Antioxidative activity of $FePS_3$ NSs by PTIO assay compared with a typical antioxidant (Trolox). (f) Percentage of Fe, P, and S at different valence states in three groups: (I) $FePS_3$ NSs in ethanol, (II) $FePS_3$ NSs in PBS (pH 7.4), (III) $FePS_3$ NSs + H_2O_2 in PBS (pH 7.4). Inset: Photographs of the samples. (g) EPR spectra of the DMPO + Fe^{2+}/H_2O_2 mixtures with the presence of $FePS_3$ NSs at pH 7.4.

The time-dependent absorbance of $FePS_3$ NSs (at 375 nm) was monitored under different pH conditions, and the corresponding dissolution percentage was calculated based on the decrease of absorbance over time (Fig. S5 and S6, ESI†). As shown in Fig. 2c, $FePS_3$ NSs show little dissolution under neutral conditions, while they can completely dissolve under acidic conditions. As previously reported, $FePS_3$ is formed based on the ionic bonds between Fe cations and $[P_2S_6]^{4-}$, which may influence their dissociation at different pH conditions.[49,53] Besides, XPS analysis (Fig. S7, ESI†) demonstrates no obvious change on the valence states of the elements in $FePS_3$ NSs whether dispersed in aqueous solutions with different pH conditions (5.0 or 7.4), suggesting that the decreased absorbance of $FePS_3$ NSs is related to the dissociation of $FePS_3$ rather than the oxidative decomposition by the dissolved oxygen. These results reveal that $FePS_3$ NSs may dissolve and release Fe^{2+} cations and $[P_2S_6]^{4-}$ anions in response to the acidic environment while keeping stable under neutral conditions.

The acid-responsive Fe^{2+} release can account for the acid-responsive Fenton activity of $FePS_3$ NSs (eqn (1) and (2)), while the $[P_2S_6]^{4-}$ also exerts an essential function in Fenton reaction.

 This journal is © The Royal Society of Chemistry 2021

Published on 23 1 2021. Downloaded on 2024-08-16 4:52:42.

XPS analysis was performed to investigate the changes in the valence states of Fe/P/S in $FePS_3$ NSs after reaction with different amounts of H_2O_2 at pH 5.0. As Fig. 2d and Fig. S8 (ESI†) show, when the amount of H_2O_2 added is less than 100 eq. of $FePS_3$, the decrease of Fe(II) and increase of Fe(III) is limited. At the same time, the oxidation of P(IV) and S(−II) gradually increases. Once the $[P_2S_6]^{4-}$ anions are completely consumed, the conversion of Fe(II) to Fe(III) begins. Also, all the $FePS_3$ + H_2O_2 mixtures carry on Fenton reaction, whether the oxidation of $[P_2S_6]^{4-}$ is complete (Fig. S9, ESI†), indicating that $[P_2S_6]^{4-}$ can reduce the as-formed Fe^{3+} to Fe^{2+} during the Fenton reaction until depletion (eqn (3) and (4)). Thus, $[P_2S_6]^{4-}$ may participate in the iron redox cycling in the Fenton reaction, which can enhance the Fenton activity of $FePS_3$ NSs.

$$2FePS_3 \rightarrow 2Fe^{2+} + [P_2S_6]^{4-} \quad (1)$$

$$Fe^{2+} + H_2O_2 \rightarrow Fe^{3+} + {}^{\bullet}OH + OH^- \quad (2)$$

$$[P_2S_6]^{4-} + 14Fe^{3+} + 8H_2O \rightarrow 14Fe^{2+} + 2PO_4{}^{3-} + 6S + 16H^+ \quad (3)$$

$$[P_2S_6]^{4-} + 50Fe^{3+} + 32H_2O \rightarrow 50Fe^{2+} + 2PO_4{}^{3-} + 6SO_4{}^{2-} + 64H^+ \quad (4)$$

$$FePS_3 + 4H_2O_2 \rightarrow Fe^{3+} + PO_4{}^{3-} + 3S + 4H_2O \quad (5)$$

Under neutral condition, $FePS_3$ NSs have neglectable Fenton activity due to the limited release of Fe^{2+} and acid-dependent Fenton activity, while the reductive $[P_2S_6]^{4-}$ potentially endows $FePS_3$ NSs with ROS scavenging ability. Thus, 2-phenyl-4,4,5,5-tetramethylimidazolinium-3-oxo-1-oxo (PTIO) radicals (PTIO$^{\bullet}$) and 2,2′-biazinobis(3-ethylbenzothiazoline-6-sulfonic acid) (ABTS) radicals ($ABTS^{+\bullet}$) were used to test the antioxidative activity of $FePS_3$ NSs.[56,57] As Fig. 2e shows, the PTIO$^{\bullet}$ scavenging capability of $FePS_3$ NSs is about 3.2 times as high as that of a typical antioxidant (6-hydroxy-2,5,7,8-tetramethychroman-2-carboxylic acid, Trolox). Similarly, $FePS_3$ NSs also exhibit significant scavenging ability towards $ABTS^{+\bullet}$, which is about 2.4 times that of Trolox (Fig. S10, ESI†). These results indicate the excellent antioxidative activity of $FePS_3$ NSs. Moreover, the scavenging ability of $FePS_3$ NSs for typical ROS (H_2O_2 and $^{\bullet}OH$) in a biological system was further studied.[58] As Fig. 2f illustrates, the addition of H_2O_2 into the $FePS_3$ NS solution (pH 7.4) leads to significant colour fading without the generation of oxygen bubbles or $^{\bullet}OH$ (Fig. 2a and b). Corresponding XPS analysis shows that the Fe(II), P(IV) and S(−II) in $FePS_3$ NSs were oxidized to form Fe(III), P(V) and S(0) (Fig. 2f and Fig. S11, ESI†), which suggests that $FePS_3$ NSs may eliminate H_2O_2 through redox reaction as shown in eqn (5). In addition, $^{\bullet}OH$ was generated *via* the Fe^{2+}/H_2O_2 system to investigate the $^{\bullet}OH$ scavenging capability of $FePS_3$ NSs. EPR results show that the intensity of the DMPO/$^{\bullet}OH$ signal dramatically decreases with the addition of $FePS_3$ NSs, indicating the elimination of $^{\bullet}OH$ (Fig. 2g). Salicylic acid (SA), a $^{\bullet}OH$ specific probe with a characteristic absorption peak at 510 nm after reaction with $^{\bullet}OH$, was also utilized.[59] The absorbance of the SA + Fe^{2+}/H_2O_2 + $FePS_3$ NSs mixture is much lower than that of the SA + Fe^{2+}/H_2O_2 mixture, and the calculated elimination percentage of $^{\bullet}OH$ rises gradually with increasing concentrations of $FePS_3$ NSs, revealing their $^{\bullet}OH$ scavenging properties (Fig. S12, ESI†). Hence, $FePS_3$ NSs possess antioxidative activity to effectively scavenge H_2O_2 and $^{\bullet}OH$ in neutral conditions.

The acid-responsive self-enhanced Fenton activity of $FePS_3$ NSs was further examined for the treatment of both planktonic bacteria and bacterial biofilms. The bacterial growth curves of *Staphylococcus aureus* (*S. aureus*) treated with $FePS_3$ NSs show a significant bacteriostatic effect either without or with H_2O_2 (Fig. S13a and b, ESI†). Also, the bacterial growth inhibition effect of $FePS_3$ NSs + H_2O_2 is much higher than that of $FePS_3$ NSs, indicating enhanced antibacterial activity of $FePS_3$ NSs *via* Fenton reaction. On the other hand, the inactivation efficiency of $FePS_3$ NSs (50 μg mL^{-1}) against planktonic *S. aureus* reached 4.2 log (~99.99%) and 6.2 log (~99.9999%) without and with H_2O_2 (100 μM), respectively, which reveals the good antibacterial activity of $FePS_3$ NSs (Fig. S13c and d, ESI†).[60–63] Moreover, *S. aureus* biofilms were further challenged by $FePS_3$ NSs to investigate the *in vitro* anti-biofilm effect. Extra H_2O_2 (100 μM) was introduced to mimic the *in vivo* biofilm microenvironment.[64,65] The ROS level in biofilms was measured using 2′,7′-dichlorodihydrofluorescein diacetate (DCFH-DA).[64,66,67] As shown in the 3D confocal laser scanning microscopy (CLSM) images, the fluorescence intensity of the *S. aureus* biofilms treated by $FePS_3$ NSs + H_2O_2 is much higher than those treated by H_2O_2 or $FePS_3$ NSs (Fig. 3a and Fig. S14a, ESI†), indicating the generation of $^{\bullet}OH$ caused by Fenton-active $FePS_3$ NSs. Moreover, calcein acetoxymethyl ester (calcein-AM) was used to stain live bacteria in *S. aureus* biofilms. Among them, biofilms treated by $FePS_3$ NSs + H_2O_2 show the lowest fluorescence intensity (Fig. 3a and Fig. S14b, ESI†), demonstrating their excellent bacterial killing effect in biofilms. As shown in Fig. 3b, the bacterial inactivation efficiency of H_2O_2 (100 μM) alone is only 0.13 log (~25.89%), while that of $FePS_3$ NSs with lower concentration (27 μM, 5 μg mL^{-1}) is 0.28 log (~47.64%), indicating the better anti-biofilm effect of $FePS_3$ NSs compared with H_2O_2. Besides, the colony-forming units (CFU) number of bacteria in biofilms treated by $FePS_3$ NSs (50 μg mL^{-1}) with H_2O_2 (100 μM) decreased by about 4 log (~99.99%) and the CFU number of the group treated by only $FePS_3$ NSs (50 μg mL^{-1}) decreased by less than 2 log (~98.62%), which revealed the excellent sterilization of $^{\bullet}OH$ generated *via* $FePS_3$ NSs through Fenton reaction. In addition, crystal violet staining was conducted after different treatments to evaluate the total biofilm biomass including bacteria and EPS. Compared with the sole treatment of H_2O_2 or $FePS_3$ NSs, the *S. aureus* biofilms treated by H_2O_2 + $FePS_3$ NSs show much less biomass (Fig. S15, ESI†). As the quantitative analysis shows in Fig. 3c, the relative biofilm biomass is reduced to about 24% after the treatment of $FePS_3$ NSs (50 μg mL^{-1}) with the presence of H_2O_2 (100 μM), much lower than that of H_2O_2 (~95%) or $FePS_3$ NSs (~50%). The morphology of the biofilms after different treatments was studied by SEM images (Fig. 3d). *S. aureus* inside biofilms without treatment presents sphere-like morphology with smooth and intact cell walls, while the bacterial surface becomes distorted and wrinkled in the $FePS_3$ NSs + H_2O_2 group. These results demonstrate that $FePS_3$ NSs have excellent

Published on 23 1 2021. Downloaded on 2024-08-16 4:52:42.

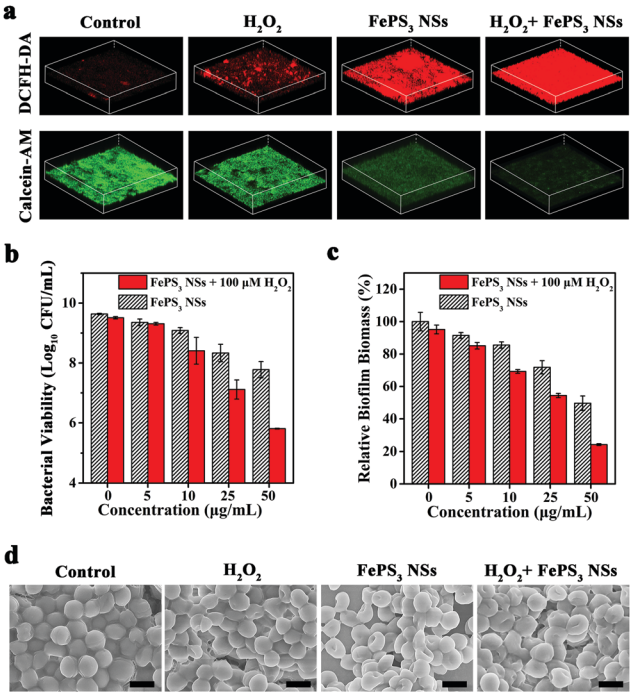

Fig. 3 *In vitro* anti-biofilm effect of $FePS_3$ NSs. (a) 3D CLSM images of *S. aureus* biofilms treated with saline (control), 100 μM H_2O_2, 25 μg mL^{-1} $FePS_3$ NSs, and 25 μg mL^{-1} $FePS_3$ NSs + 100 μM H_2O_2, respectively. Calcein-AM is used to dye live bacteria in biofilms, and the ROS level is imaged by using DCFH-DA as the fluorescent probe. (630 μm × 630 μm) (b) The CFU number of bacteria and (c) relative biofilm biomass of *S. aureus* biofilms after treated by different concentrations of $FePS_3$ NSs with or without H_2O_2. (d) SEM images of *S. aureus* biofilms after being treated with saline, 100 μM H_2O_2, 50 μg mL^{-1} $FePS_3$ NSs, and 50 μg mL^{-1} $FePS_3$ NSs + 100 μM H_2O_2, respectively. The scale bar is 400 μm.

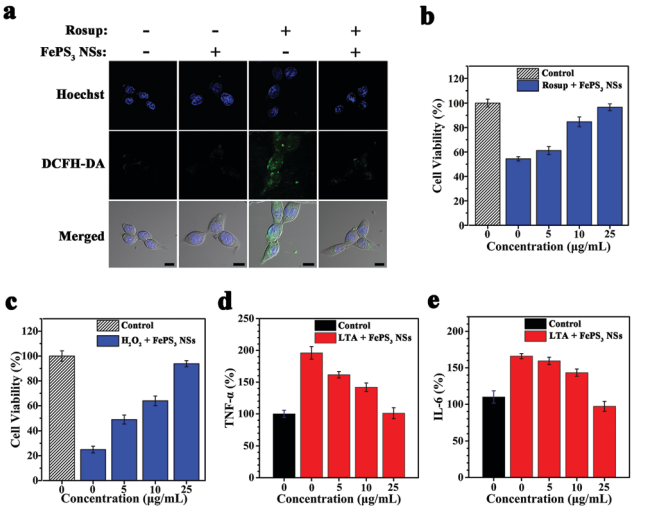

Fig. 4 *In vitro* ROS scavenging and anti-inflammatory effect of $FePS_3$ NSs. (a) CLSM images of NIH-3T3 cells after different treatments. Hochest 33342 and DCFH-DA were used to stain the cell nucleus and detect the intracellular ROS level, respectively. The scale bar is 10 μm. Cell viability of NIH-3T3 cells treated by $FePS_3$ NSs with different concentrations under the stimulation of (b) Rosup or (c) H_2O_2. (d) TNF-α and (e) IL-6 levels in RAW264.7 cells treated by $FePS_3$ NSs with different concentrations under the stimulation of LTA.

anti-biofilm effect in response to the acid and H_2O_2 in the biofilm microenvironment by self-enhanced Fenton activity.

The cytotoxicity of $FePS_3$ NSs was first studied using murine fibroblast (NIH-3T3) cells. After incubation with $FePS_3$ NSs at the concentration up to 80 μg mL^{-1}, no obvious decrease in the viability of NIH-3T3 cells can be observed (Fig. S16a, ESI†). Besides, $FePS_3$ NSs exhibit low hemolysis effect, indicating their good blood compatibility (Fig. S16b, ESI†). Furthermore, the *in vivo* toxicity of $FePS_3$ NSs was assessed in healthy mice by tail vein injection (~1 mg kg^{-1}). The body weights of the mice injected with $FePS_3$ NSs have no noticeable difference from those injected with saline (0.85% NaCl) (Fig. S16c, ESI†). Hematoxylin and eosin (H&E) staining images show that the major organs from these mice have no observable damage post-injection for 21 days (Fig. S16d, ESI†). Meanwhile, there are no abnormal results in both hematology assay and liver/kidney function markers (Fig. S17, ESI†). Therefore, $FePS_3$ NSs have negligible toxicity to mice at the dose used in this work.

To evaluate the *in vitro* ROS scavenging properties of $FePS_3$ NSs, NIH-3T3 cells were pretreated with Rosup to induce intracellular ROS generation, and then treated with $FePS_3$ NSs.[59,68] The fluorescence intensity of NIH-3T3 cells stained with DCFH-DA decreases significantly upon the addition of $FePS_3$ NSs (Fig. 4a and Fig. S18, ESI†), suggesting the lowered intracellular ROS level.[69] The cell viability of NIH-3T3 cells treated by Rosup decreased to 55% due to the oxidative stress (Fig. 4b). In comparison, the viability of NIH-3T3 cells stimulated by Rosup and followed by $FePS_3$ NS treatment remained up to 95%, which indicates the cell protection effect of $FePS_3$ NSs from excessive ROS. Besides, when H_2O_2 was used to induce oxidative damage to NIH-3T3 cells, the pretreatment by $FePS_3$ NSs can also efficiently protect them from oxidative stress (Fig. 4c). These results suggest that $FePS_3$ NSs are an effective ROS scavenger for the relief of oxidative stress. On the other hand, since ROS can act as a secondary cellular messenger for inflammatory cytokine signalling, the anti-inflammatory effect of $FePS_3$ NSs by ROS scavenging was further studied.[70,71] Lipoteichoic acid (LTA) was employed to stimulate murine macrophage (RAW264.7) cells to induce an *in vitro* inflammatory response. After the treatment, tumour necrosis factor-α (TNF-α) and interleukin-6 (IL-6) were tested as inflammation markers. Pretreatment with $FePS_3$ NSs significantly reduced both the TNF-α level and IL-6 level (Fig. 4d and e), suggesting reduced inflammation. Hence, $FePS_3$ NSs may mitigate the oxidative stress and inflammation in normal tissues by scavenging excessive ROS.

Considering the difference of pH conditions between biofilm infected tissues and normal tissues, $FePS_3$ NSs are expected to have microenvironment-selective anti-biofilm and anti-inflammatory effects. The *in vivo* therapeutic efficacy of $FePS_3$ NSs was studied on *S. aureus* biofilm infected mice models (Fig. 5a). One day after infection, $FePS_3$ NSs (~0.5 mg kg^{-1}) and saline (control) were *in situ* injected into the abscesses of infected mice, respectively.

 This journal is © The Royal Society of Chemistry 2021

Published on 23 1 2021. Downloaded on 2024-08-16 4:52:42.

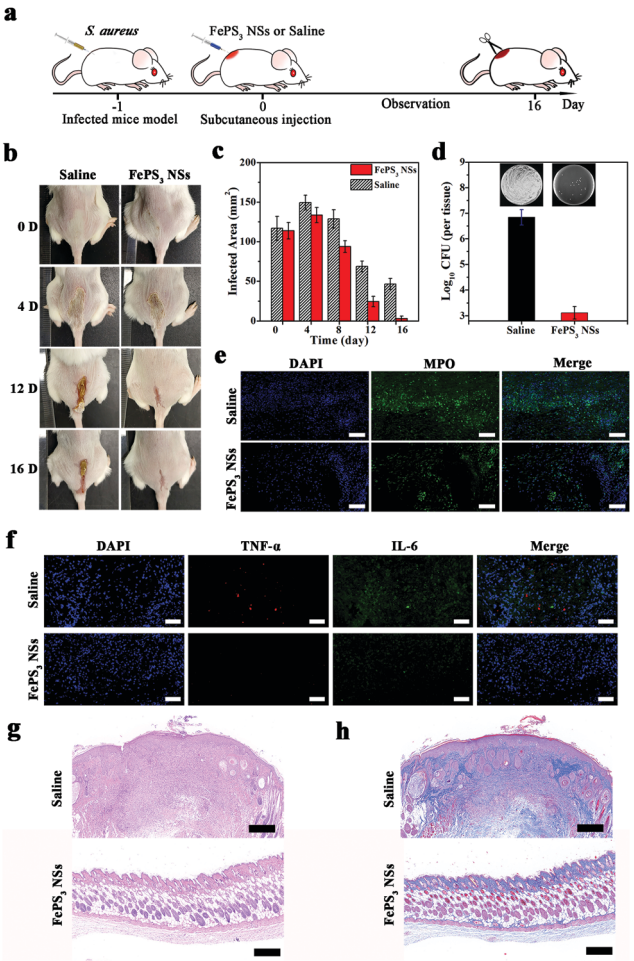

Fig. 5 Treatment of *S. aureus* biofilm infected mice by $FePS_3$ NSs. (a) Schematic illustration of the treatment process. (b) Photographs of the infected tissues after different treatments. (c) The change of infected area at different time points post-treatment. (d) CFU number of surviving bacteria in the infected tissues at the 16th-day post-treatment. Inset: Photographs of agar plates. (e) Infiltration of neutrophils in the infected tissues characterized by immunofluorescence staining of MPO (MPO: green; nuclei: blue). The cell nuclei were stained by DAPI (4′,6-diamidino-2-phenylindole). The scale bar is 200 μm. (f) Immunofluorescence staining images of TNF-α and IL-6 in the infected tissues (nuclei: blue; TNF-α: red; IL-6: green). The scale bar is 50 μm. (g) H&E and (h) Masson's trichrome staining images of the infected tissues. The scale bar is 500 μm.

As illustrated in Fig. 5b and c, the infected areas of the mice treated with $FePS_3$ NSs are much smaller than that of the mice treated by saline. At the 16th-day post-treatment with $FePS_3$ NSs, the abscesses and wound beds of mice almost disappear, which indicates that $FePS_3$ NSs can effectively facilitate the recovery of *S. aureus* biofilm infected tissues. As shown in Fig. 5d, the number of live *S. aureus* in the infected tissues was quantified, and the bacterial inactivation efficiency of $FePS_3$ NSs is about 3.7 log (99.98%), suggesting an excellent *in vivo* anti-biofilm effect of $FePS_3$ NSs. Moreover, neutrophils in the infected tissues were detected by immunofluorescence staining of myeloperoxidase (MPO).[72,73] Strong fluorescence can be clearly observed in the infected tissues of the saline group, while that of the $FePS_3$ NS group is remarkably reduced, indicating fewer neutrophils infiltration and reduced inflammation (Fig. 5e). Meanwhile, the expressions of typical pro-inflammatory cytokines (TNF-α and IL-6) in the infected tissues treated by $FePS_3$ NSs show a significant reduction, which further confirms the *in vivo* anti-inflammatory effect of $FePS_3$ NSs (Fig. 5f). The therapeutic efficiency of $FePS_3$ NSs towards *S. aureus* biofilm infected mice was also evaluated by histological analysis. As the H&E staining images (Fig. 5g) show, the infiltration of plenty of inflammatory cells indicates that the intensive inflammation still remained in the infected tissues of the saline group. In contrast, fewer inflammatory cells and a more intact epidermis layer can be observed in the $FePS_3$ NS group. Besides, Masson's trichrome staining images (Fig. 5h) for the $FePS_3$ NS group show better collagen fiber formation in the infected tissues. These results demonstrate that $FePS_3$ NSs exhibit excellent anti-biofilm and anti-inflammatory efficacy in the *S. aureus* biofilm infected mice.

Conclusions

In summary, $FePS_3$ NSs possess both self-enhanced Fenton activity under acidic conditions and ROS scavenging properties under neutral conditions. As a pH-responsive multifunctional Fenton nanoagent, $FePS_3$ NSs exhibit microenvironment-selective anti-biofilm and anti-inflammatory effects against bacterial biofilm infections. In bacterial biofilms with an acidic microenvironment, $FePS_3$ NSs can release Fe^{2+} and react with H_2O_2 by Fenton reaction to generate Fe^{3+} and highly oxidative $^{\bullet}OH$ for bacteria-killing in biofilms; while the $[P_2S_6]^{4-}$ can reduce the as-formed Fe^{3+} to Fe^{2+}, which significantly enhances the therapeutic effect of the Fenton reaction by promoting iron redox cycling. In normal tissues with neutral pH, $FePS_3$ NSs exhibit effective ROS scavenging properties *via* the reductive $[P_2S_6]^{4-}$, which can relieve oxidative stress and exert an anti-inflammation effect. Both *in vitro* and *in vivo* experimental results demonstrate that $FePS_3$ NSs can simultaneously eradicate bacterial biofilms and mitigate tissue inflammation, and achieve excellent therapeutic efficacy for bacterial biofilm infections. Besides, $FePS_3$ NSs show good biocompatibility with neglectable toxicity to mice. Overall, this work demonstrates that the integration of Fe cations and reductive anions in one Fenton agent makes $FePS_3$ NSs a kind of novel pH-responsive therapeutic nanoagent with self-enhanced Fenton activity and ROS scavenging properties, facilitating the microenvironment-selective anti-biofilm and anti-inflammatory therapy for bacterial biofilm infections.

Authors' contributions

L. Wang and L. Yuwen conceived the idea and supervised the study. Y. Li carried out the experiments, analysed the results, and wrote the manuscript. W. Xiu, K. Yang, Q. Wen and Z. Luo helped with the experimental characterization and the results discussion. D. Yang supported the operation of animal

Published on 23 1 2021. Downloaded on 2024-08-16 4:52:42.

experiments. X. Liu and X. Xie contributed to the scientific discussion of the manuscript. All authors discussed, commented and agreed on the manuscript.

Conflicts of interest

The authors declare no conflict of interest.

Acknowledgements

This work was financially supported by the National Key Research and Development Program of China (2017YFA0205302), the Natural Science Foundation of Jiangsu Province (BK20191382), the Key Research and Development Program of Jiangsu (BE2018732), the Natural Science Key Fund for Colleges and Universities in Jiangsu Province (17KJA430011), and the Priority Academic Program Development of Jiangsu Higher Education Institutions (PAPD, YX030003).

References

1 J. W. Costerton, P. S. Stewart and E. P. Greenberg, *Science*, 1999, **284**, 1318.
2 R. A. Fisher, B. Gollan and S. Helaine, *Nat. Rev. Microbiol.*, 2017, **15**, 453–464.
3 H. Flemming, J. Wingender, U. Szewzyk, P. Steinberg, S. A. Rice and S. Kjelleberg, *Nat. Rev. Microbiol.*, 2016, **14**, 563–575.
4 F. Sun, F. Qu, Y. Ling, P. Mao, P. Xia, H. Chen and D. Zhou, *Future Microbiol.*, 2013, **8**, 877–886.
5 N. Høiby, T. Bjarnsholt, M. Givskov, S. Molin and O. Ciofu, *Int. J. Antimicrob. Agents*, 2010, **35**, 322–332.
6 H.-C. Flemming and J. Wingender, *Nat. Rev. Microbiol.*, 2010, **8**, 623–633.
7 T. Bjarnsholt, M. Alhede, M. Alhede, S. R. Eickhardt-Sorensen, C. Moser, M. Kuhl, P. O. Jensen and N. Hoiby, *Trends Microbiol.*, 2013, **21**, 466–474.
8 N. Hoiby, T. Bjarnsholt, C. Moser, G. L. Bassi, T. Coenye, G. Donelli, L. Hall-Stoodley, V. Hola, C. Imbert, K. Kirketerp-Moller, D. Lebeaux, A. Oliver, A. J. Ullmann, C. Williams, E. S. G. f. Biofilms and Z. Consulting External Expert Werner, *Clin. Microbiol. Infect.*, 2015, **21**, 1–25.
9 P. S. Stewart and M. J. Franklin, *Nat. Rev. Microbiol.*, 2008, **6**, 199–210.
10 Z. Tang, Y. Liu, M. He and W. Bu, *Angew. Chem., Int. Ed.*, 2019, **58**, 946–956.
11 H. Ranji-Burachaloo, P. A. Gurr, D. E. Dunstan and G. G. Qiao, *ACS Nano*, 2018, **12**, 11819–11837.
12 J. A. Lemire, J. J. Harrison and R. J. Turner, *Nat. Rev. Microbiol.*, 2013, **11**, 371–384.
13 X. Ji, Y. Kang, J. Ouyang, Y. Chen, D. Artzi, X. Zeng, Y. Xiao, C. Feng, B. Qi, N. Y. Kim, P. E. Saw, N. Kong, O. C. Farokhzad and W. Tao, *Adv. Sci.*, 2019, **6**, 1901211.
14 N. Kong, X. Ji, J. Wang, X. Sun, G. Chen, T. Fan, W. Liang, H. Zhang, A. Xie, O. C. Farokhzad and W. Tao, *Nano Lett.*, 2020, **20**, 3943–3955.
15 E. Linley, S. P. Denyer, G. McDonnell, C. Simons and J. Y. Maillard, *J. Antimicrob. Chemother.*, 2012, **67**, 1589–1596.
16 J. A. Imlay and S. Linn, *Science*, 1988, **240**, 1302–1309.
17 J. Tamarit, E. Cabiscol and J. Ros, *J. Biol. Chem.*, 1998, **273**, 3027–3032.
18 F. C. Fang, *Nat. Rev. Microbiol.*, 2004, **2**, 820–832.
19 J. Shan, X. Li, K. Yang, W. Xiu, Q. Wen, Y. Zhang, L. Yuwen, L. Weng, Z. Teng and L. Wang, *ACS Nano*, 2019, **13**, 13797–13808.
20 Z. He, X. Huang, C. Wang, X. Li, Y. Liu, Z. Zhou, S. Wang, F. Zhang, Z. Wang, O. Jacobson, J. J. Zhu, G. Yu, Y. Dai and X. Chen, *Angew. Chem., Int. Ed.*, 2019, **58**, 8752–8756.
21 M. Song, Y. Cheng, Y. Tian, C. Chu, C. Zhang, Z. Lu, X. Chen, X. Pang and G. Liu, *Adv. Funct. Mater.*, 2020, 2003587, DOI: 10.1002/adfm.202003587.
22 S. C. Park, N. H. Kim, W. Yang, J. W. Nah, M. K. Jang and D. Lee, *J. Controlled Release*, 2016, **221**, 37–47.
23 X. Cheng, S. Zhang, H. Liu, H. Chen, J. Zhou, Z. Chen, X. Zhou, Z. Xie, Q. Kuang and L. Zheng, *ACS Appl. Mater. Interfaces*, 2020, **12**, 36996–37005.
24 L. Wang, Y. Miao, M. Lu, Z. Shan, S. Lu, J. Hou, Q. Yang, X. Liang, T. Zhou, D. Curry, K. Oakes and X. Zhang, *Chem. Commun.*, 2017, **53**, 5862–5865.
25 A. D. Bokare and W. Choi, *J. Hazard. Mater.*, 2014, **275**, 121–135.
26 H. Dong, C. Sans, W. Li and Z. Qiang, *Sep. Purif. Technol.*, 2016, **171**, 144–150.
27 S. Zhang, M. Sun, T. Hedtke, A. Deshmukh, X. Zhou, S. Weon, M. Elimelech and J. H. Kim, *Environ. Sci. Technol.*, 2020, **54**, 10868–10875.
28 B. Shen, C. Dong, J. Ji, M. Xing and J. Zhang, *Chin. Chem. Lett.*, 2019, **30**, 2205–2210.
29 H. Sun, G. Xie, D. He and L. Zhang, *Appl. Catal., B*, 2020, **267**, 118383.
30 P. Zhao, Z. Tang, X. Chen, Z. He, X. He, M. Zhang, Y. Liu, D. Ren, K. Zhaoe and W. Bu, *Mater. Horiz.*, 2019, **6**, 369–374.
31 P. Poprac, K. Jomova, M. Simunkova, V. Kollar, C. J. Rhodes and M. Valko, *Trends Pharmacol. Sci.*, 2017, **38**, 592–607.
32 T. P. A. Devasagayam, J. C. Tilak, K. K. Boloor, K. Sane, S. Ghaskadbi and R. Lele, *J. Assoc. Physicians India*, 2004, **52**, 794–804.
33 A. Scalise, A. Bianchi, C. Tartaglione, E. Bolletta, M. Pierangeli, M. Torresetti, M. Marazzi and G. Di Benedetto, *Semin. Vasc. Surg.*, 2015, **28**, 151–159.
34 W. Xiu, J. Shan, K. Yang, H. Xiao, L. Yuwen and L. Wang, *View*, 2020, 20200065, DOI: 10.1002/viw.20200065.
35 L. Chen and Y.-m. Wen, *Int. J. Oral Sci.*, 2011, **3**, 66–73.
36 P. O. Jensen, M. Kolpen, K. N. Kragh and M. Kuhl, *Acta Pathol., Microbiol. Immunol. Scand.*, 2017, **125**, 276–288.
37 S. Sivakanesan and E. A. Dawes, *J. Gen. Microbiol.*, 1980, **118**, 143–157.
38 D. S. Benoit and H. Koo, *Nanomedicine*, 2016, **11**, 873–879.
39 W. Xiu, S. Gan, Q. Wen, Q. Qiu, S. Dai, H. Dong, Q. Li, L. Yuwen, L. Weng, Z. Teng, Y. Mou and L. Wang, *Research*, 2020, 9426453, DOI: 10.34133/2020/9426453.
40 D. S. Benoit and H. Koo, *Nanomedicine*, 2016, **11**, 873–879.

 This journal is © The Royal Society of Chemistry 2021

Published on 23 1 2021. Downloaded on 2024-08-16 4:52:42.

41 Q. Deng, P. Sun, L. Zhang, Z. Liu, H. Wang, J. Ren and X. Qu, *Adv. Funct. Mater.*, 2019, **29**, 1903018.
42 J. Wu, F. Li, X. Hu, J. Lu, X. Sun, J. Gao and D. Ling, *ACS Cent. Sci.*, 2019, **5**, 1366–1376.
43 L. Su, Y. Li, Y. Liu, R. Ma, Y. Liu, F. Huang, Y. An, Y. Ren, H. C. Mei, H. J. Busscher and L. Shi, *Adv. Funct. Mater.*, 2020, **30**, 2000537.
44 D. Hu, Y. Deng, F. Jia, Q. Jin and J. Ji, *ACS Nano*, 2020, **14**, 347–359.
45 Y. Shi, J. Yin, Q. Peng, X. Lv, Q. Li, D. Yang, X. Song, W. Wang and X. Dong, *Biomater. Sci.*, 2020, **8**, 6093–6099.
46 X. Lv, J. Zhang, D. Yang, J. Shao, W. Wang, Q. Zhang and X. Dong, *J. Mater. Chem. B*, 2020, **8**, 10700–10711.
47 D. Mukherjee, P. M. Austeria and S. Sampath, *ACS Energy Lett.*, 2016, **1**, 367–372.
48 Z. Cheng, T. A. Shifa, F. Wang, Y. Gao, P. He, K. Zhang, C. Jiang, Q. Liu and J. He, *Adv. Mater.*, 2018, **30**, 1707433.
49 F. Wang, T. A. Shifa, P. Yu, P. He, Y. Liu, F. Wang, Z. Wang, X. Zhan, X. Lou, F. Xia and J. He, *Adv. Funct. Mater.*, 2018, **28**, 1802151.
50 P. A. Joy and S. Vasudevan, *J. Phys. Chem. Solids*, 1993, **54**, 343–348.
51 N. Ismail, A. A. El-Meligi, Y. M. Temerkb and M. Madian, *Int. J. Hydrogen Energy*, 2010, **35**, 7827–7834.
52 W. Zhu, W. Gan, Z. Muhammad, C. Wang, C. Wu, H. Liu, D. Liu, K. Zhang, Q. He, H. Jiang, X. Zheng, Z. Sun, S. Chen and L. Song, *Chem. Commun.*, 2018, **54**, 4481–4484.
53 R. Gusmão, Z. Sofer and M. Pumera, *Angew. Chem., Int. Ed.*, 2019, **58**, 9326–9337.
54 L. Gao, J. Zhuang, L. Nie, J. Zhang, Y. Zhang, N. Gu, T. Wang, J. Feng, D. Yang, S. Perrett and X. Yan, *Nat. Nanotechnol.*, 2007, **2**, 577–583.
55 W. Zhang, S. Hu, J. J. Yin, W. He, W. Lu, M. Ma, N. Gu and Y. Zhang, *J. Am. Chem. Soc.*, 2016, **138**, 5860–5865.
56 X. Li, *J. Agric. Food Chem.*, 2017, **65**, 6288–6297.
57 R. Re, N. Pellegrini, A. Proteggente, A. Pannala, M. Yang and C. Rice-Evans, *Free Radical Biol. Med.*, 1999, **26**, 1231–1237.
58 A. Karakoti, S. Singh, J. M. Dowding, S. Seal and W. T. Self, *Chem. Soc. Rev.*, 2010, **39**, 4422–4432.
59 J. Yao, Y. Cheng, M. Zhou, S. Zhao, S. Lin, X. Wang, J. Wu, S. Lia and H. Wei, *Chem. Sci.*, 2018, **9**, 2927–2933.
60 Y. Qiao, X. Liu, B. Li, Y. Han, Y. Zheng, K. W. K. Yeung, C. Li, Z. Cui, Y. Liang, Z. Li, S. Zhu, X. Wang and S. Wu, *Nat. Commun.*, 2020, **11**, 4446.
61 J. Ouyang, X. Ji, X. Zhang, C. Feng, Z. Tang, N. Kong, A. Xie, J. Wang, X. Sui, L. Deng, Y. Liu, J. S. Kim, Y. Cao and W. Tao, *Proc. Natl. Acad. Sci. U. S. A.*, 2020, **117**, 28667–28677.
62 J. Li, X. Liu, L. Tan, Z. Cui, X. Yang, Y. Liang, Z. Li, S. Zhu, Y. Zheng, K. W. K. Yeung, X. Wang and S. Wu, *Nat. Commun.*, 2019, **10**, 4490.
63 L. Tan, J. Li, X. Liu, Z. Cui, X. Yang, K. W. K. Yeung, H. Pan, Y. Zheng, X. Wang and S. Wu, *Small*, 2018, **14**, 1703197.
64 Z. Wang, K. Dong, Z. Liu, Y. Zhang, Z. Chen, H. Sun, J. Ren and X. Qu, *Biomaterials*, 2017, **113**, 145–157.
65 Z. Chen, Z. Wang, J. Ren and X. Qu, *Acc. Chem. Res.*, 2018, **51**, 789–799.
66 C. Zhang, W. Bu, D. Ni, S. Zhang, Q. Li, Z. Yao, J. Zhang, H. Yao, Z. Wang and J. Shi, *Angew. Chem., Int. Ed.*, 2016, **55**, 2101–2106.
67 J. Shan, K. Yang, W. Xiu, Q. Qiu, S. Dai, L. Yuwen, L. Weng, Z. Teng and L. Wang, *Small*, 2020, **16**, 2001099.
68 Y. Huang, Z. Liu, C. Liu, E. Ju, Y. Zhang, J. Ren and X. Qu, *Angew. Chem., Int. Ed.*, 2016, **55**, 6646–6650.
69 Z. Zhang, W. Sang, L. Xie, W. Li, B. Li, J. Li, H. Tian, Z. Yuan, Q. Zhao and Y. Dai, *Angew. Chem., Int. Ed.*, 2021, **60**, 1967–1975.
70 L. Shan, W. Fan, W. Wang, W. Tang, Z. Yang, Z. Wang, Y. Liu, Z. Shen, Y. Dai, S. Cheng, O. Jacobson, K. Zhai, J. Hu, Y. Ma, D. O. Kiesewetter, G. Gao and X. Chen, *ACS Nano*, 2019, **13**, 8903–8916.
71 F. Vatansever1, W. C. M. A. d. Melo, P. Avci, D. Vecchio, M. Sadasivam, A. Gupta, R. Chandran, M. Karimi, N. A. Parizotto, R. Yin, G. P. Tegos and M. R. Hamblin, *FEMS Microbiol. Rev.*, 2013, **37**, 955–989.
72 J. Ouyang, M. Wen, W. Chen, Y. Tan, Z. Liu, Q. Xu, K. Zeng, L. Deng and Y.-N. Liu, *Chem. Commun.*, 2019, **55**, 4877–4880.
73 P. P. Bradley, D. A. Priebat, R. D. Christensen and G. Rothstein, *J. Invest. Dermatol.*, 1982, **78**, 206–209.